ACS APPLIED MATERIALS & INTERFACES

www.acsami.org

Research Article

Silk Fibroin-Based Multiple-Shape-Memory Organohydrogels

Cigdem Buse Oral, Esra Su, and Oguz Okay*

Cite This: ACS Appl. Mater. Interfaces 2024, 16, 56146−56158

Read Online

ACCESS | Metrics & More | Article Recommendations | Supporting Information

ABSTRACT: Organohydrogels (OHGs) are intriguing materials due to their unique composition of both hydrophilic and hydrophobic domains. This antagonistic nature endows the OHGs with several remarkable properties, making them highly versatile for various applications. We present here a simple and inexpensive approach to fabricate silk fibroin (SF)-based OHGs with multistage switching mechanics and viscoelasticity. The continuous hydrophilic phase of the OHG precursor consists of an aqueous SF solution, while the hydrophobic droplet phase consists of a crystallizable *n*-octadecyl acrylate (C18A) monomer and several long-chain saturated hydrocarbons (HCs) with various chain lengths between 14 and 32 carbon atoms, namely, *n*-tetradecane, *n*-octadecane, *n*-docosane, *n*-dotriacontane, and 1-docosanol. After the addition of a C18A/HC mixture containing Irgacure photoinitiator into the continuous aqueous SF phase under stirring, a stable oil-in-water emulsion was obtained, which was then photopolymerized at 23 ± 2 °C to obtain nonswelling OHGs with multiple-shape-memory behavior. By changing the chain length and mass proportion of HCs, a series of OHGs with tunable transition temperatures could be obtained, meeting various applications. OHGs containing dimer, trimer, and quadruple combinations of in situ-formed poly(C18A) and HC microinclusions exhibit effective triple- or quintuple-shape memory whose shape-recovery temperatures could be adjusted over a wide range, e.g., between 7 and 70 °C.

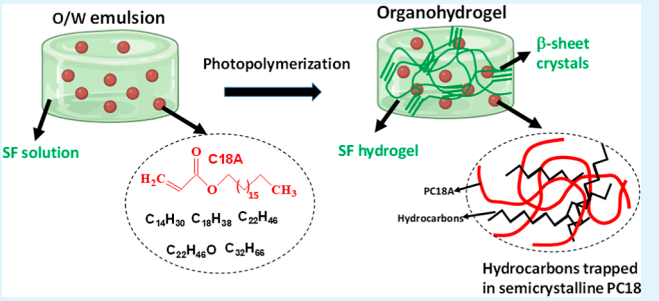

KEYWORDS: *organohydrogels, silk fibroin, emulsion, long-chain saturated hydrocarbons, n-octadecyl acrylate, shape memory*

1. INTRODUCTION

The concept of creating synthetic materials that mimic the functionality of biological systems possessing both hydrophilic and hydrophobic properties is challenging in material science.[1] These materials, termed organohydrogels (OHGs), draw inspiration from the natural world, where organisms have developed complex mechanisms to survive and thrive under diverse and often harsh conditions. The ability of sea cucumbers and starfish to alter the stiffness of their tissue is an example of how living organisms can dynamically adjust their biomechanical properties in response to environmental stimuli.[2−4] This is achieved through the nervous system controlling the properties of the collagen in their tissues, allowing them to switch between soft and rigid states. OHGs that can similarly change their mechanical properties on demand would have wide-ranging applications in robotics, prosthetics, and smart textiles.[5,6] Another example is antifreeze proteins in arctic wood frogs that have both hydrophilic and lyophilic segments, enabling the frogs to survive in freezing temperatures by preventing ice crystal formation in their bodily fluids.[7,8] Mimicking this property in synthetic materials such as OHGs could lead to the development of substances that protect biological tissue from freezing damage or new antifreeze formulations for industrial applications. Some other potential applications of OHGs are in the biomedical field (wound dressings[9] and scaffolds for tissue engineering[10]), sensors and actuators even in harsh environments,[11] water purification,[12] cosmetics and personal care,[4] efficient energy storage devices like supercapacitors and batteries,[13] and bioadhesives for medical applications.[13] We should mention that OHGs have several advantages compared to hydrogels due to their hydrophilic and hydrophobic components. For instance, freezing-induced hardening at low temperatures and evaporation-induced structural dehydration usually occur in hydrogels, leading to the loss of their functionality. In contrast, the dynamic coexistence of opposite components in the OHGs provides them elasticity and freeze tolerance. Moreover, although hydrogels with effective dual, triple, and quadruple shape-memory effects[14] and extraordinary mechanical properties were prepared,[15,16] there is a wider range of applications of shape-memory OHGs as compared to hydrogels, making them suitable for a variety of applications across different fields.

The design of OHGs with varied microstructures and smart functions thus represents a significant challenge in material science.[1,4,13] One approach to create OHGs for freeze

Received: July 28, 2024
Revised: September 23, 2024
Accepted: September 29, 2024
Published: October 7, 2024

https://doi.org/10.1021/acsami.4c12648
ACS Appl. Mater. Interfaces 2024, 16, 56146−56158

tolerance involves submerging a covalently cross-linked hydrophilic polymer in a hydrophobic monomer and then initiating in situ polymerization.[17] Another approach is physical cross-linking of aqueous poly(vinyl alcohol) solutions containing an antifreezing binary solvent leading to antifreezing, conductive, and self-healing OHGs.[18] The emulsion-based strategy is also a versatile method to prepare OHGs with tailored microstructures.[1,4] By dispersing alkanes and/or hydrophobic monomers in an aqueous solution consisting of hydrophilic monomers and an emulsion stabilizer, one may produce OHGs with tunable properties.[1,4] Multiple-shape-memory OHGs were also fabricated through in situ polymerization of an emulsion system consisting of paraffin and hydrophobic monomers dispersed in an aqueous solution of hydrophilic monomers in the presence of nanoparticles stabilizing the emulsion through the Pickering effect.[19] The published studies so far demonstrate that by carefully manipulating the microstructure and the interactions between hydrophilic and hydrophobic components, one may create OHGs with a wide range of desirable properties, demonstrating their vast potential in various technological applications.

Silk fibroin (SF) is one of the most important and widely used proteins in biomedical applications because of its excellent mechanical properties, biocompatibility, and biodegradability.[20−23] SF also acts as a natural emulsifier due to its amphiphilic multiblock copolymer character.[24] Recently, we demonstrated that SF facilitates the formation of stable oil-in-water emulsions in the preparation of OHGs without the need for additional emulsifiers.[25] This makes the process of preparing the OHGs more environmentally friendly and biocompatible. In addition, SF offers stability to the emulsion by facilitating β-sheet formation, increasing its hydrophobicity, and serving as a physical cross-linker.[26] SF-based organohydrogel (OHG) systems possessing both hydrophilic and hydrophobic domains consist of a continuous SF hydrogel or cryogel phase in which semicrystalline poly(*n*-octadecyl acrylate) (PC18A) micro-organogels are dispersed.[25−27] Because PC18A was the only component in the oleophilic phase that could create switchable mechanical and viscoelastic properties, OHGs exhibited a biphasic transition below or above around 50 °C, which is the melting temperature of PC18A. However, replacing the single crystalline phase with multiple crystalline phases in such materials would provide multiple-shape-memory behavior, a feature which widens their application as flexible electronic devices, intelligent medical devices, sensors and actuators, smart textiles, aerospace applications, and many others.[28] The ability to memorize two, three, or four temporary shapes in addition to the permanent shape is called triple-, quadruple-, or quintuple-shape-memory effects, respectively.[14] Because several discrete transitions are required to create a multishape-memory effect, tailoring the transition temperatures via altering compositions becomes more and more challenging.

We present here a simple and inexpensive approach for fabricating SF-based OHGs with multistage switching mechanics by incorporating several long-chain saturated hydrocarbons (HCs) into the PC18A microinclusions as independent functional units. By changing the chain length and mass proportion of HCs, a series of OHGs with tunable transition temperatures could be obtained, meeting various applications. The HCs and PC18A in the microinclusions of the OHG melt and crystallize at their own phase transition temperatures and create stepwise switching viscoelastic and mechanical properties. The continuous hydrophilic phase of the OHG precursor consists of an aqueous SF solution containing the *N*,*N*-dimethylacrylamide (DMAA) monomer, the *N*,*N*′-methylene(bis)acrylamide (BAAm) cross-linker, and ethanol (Scheme 1). DMAA provides flexibility to the resulting

Scheme 1. Formation of OHGs with the Multishape-Memory Effect from Aqueous Silk Fibroin Solutions Containing Hydrophobic Microinclusions

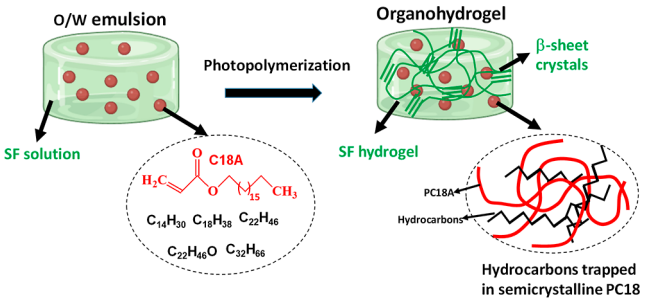

OHG, while ethanol induces conformational transition in SF from random coil to β-sheet structure and hence fibroin gelation.[25] The hydrophobic droplet phase of the OHG precursor consists of an *n*-octadecyl acrylate (C18A) monomer and HCs with various chain lengths between 14 and 32 carbon atoms, namely, *n*-tetradecane ($C_{14}H_{30}$), *n*-octadecane ($C_{18}H_{38}$), *n*-docosane ($C_{22}H_{46}$), *n*-dotriacontane ($C_{32}H_{66}$), and 1-docosanol ($C_{22}H_{46}O$) (Scheme 1). After the addition of a C18A/HC mixture containing Irgacure photoinitiator into the continuous aqueous SF phase under stirring, a stable oil-in-water emulsion was obtained, which was then photopolymerized at 23 ± 2 °C to obtain OHGs with multiple-shape-memory behavior. In the following, we first describe the condition for the formation of noneutectic PC18A/HC blends required to create the multiple-shape-memory effect in OHGs. The properties of OHGs containing dimer, trimer, and quadruple combinations of in situ-formed PC18A and HC microinclusions are then compared, and potential applications are discussed. Hereafter, organohydrogels and organohydrogel are abbreviated as OHGs and OHG, respectively.

2. RESULTS AND DISCUSSION

2.1. Neat HCs and PC18A. Figure 1a,b shows heating differential scanning calorimetry (DSC) scans of neat hydrophobic components used in this study together with their melting temperatures (T_m) and melting enthalpies (ΔH_m) plotted against their number of carbon atoms. The crystallization temperatures of the hydrophobes are given in Figure S1. Except for *n*-dotriacontane ($C_{32}H_{66}$), they all exhibit single endothermic peaks with T_m = 10, 36, 50, 53 ± 3, and 75 °C for *n*-tetradecane ($C_{14}H_{30}$), *n*-octadecane ($C_{18}H_{38}$), *n*-docosane ($C_{22}H_{46}$), PC18A, and 1-docosanol ($C_{22}H_{46}O$), respectively. $C_{32}H_{66}$ exhibits two main peaks at 69 and 73 °C due to the orthorhombic-to-hexagonal and melting transitions, respectively, while the minor peak at 46 °C is attributed to a solid−solid transition, which is an intrinsic property of commercial multi-C_n alkanes.[29] Figures 1b and S1 also show that $C_{22}H_{46}O$ and PC18A with the same chain lengths as those of $C_{22}H_{46}$ and $C_{18}H_{38}$, respectively, exhibit higher T_m and T_{cry}, indicating increasing stability of their crystalline domains, which is attributed to the steric effect of the PC18A backbone and hydrogen bonding between OH groups of $C_{22}H_{46}O$. The

https://doi.org/10.1021/acsami.4c12648
ACS Appl. Mater. Interfaces 2024, 16, 56146−56158

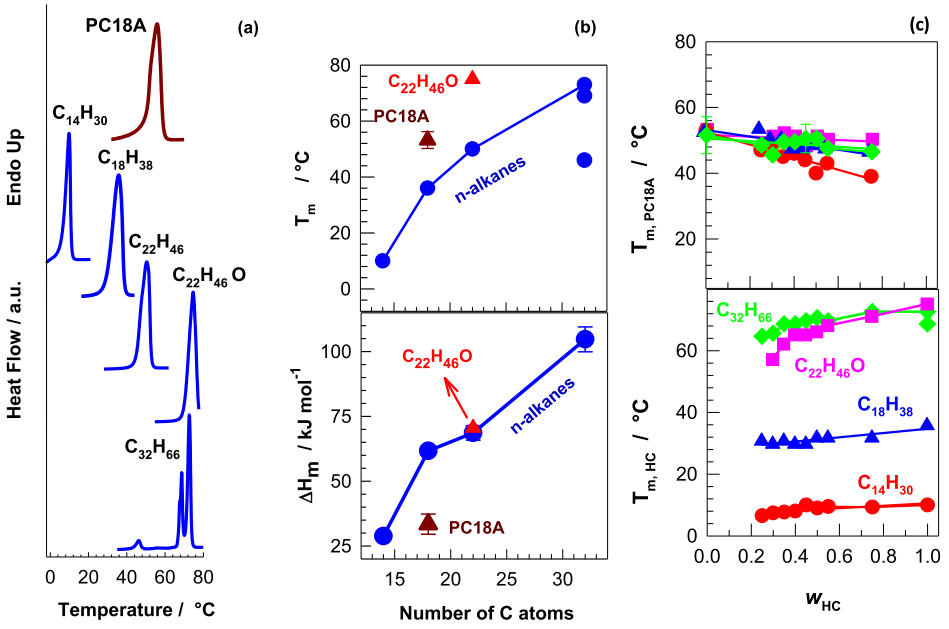

Figure 1. (a,b) Heating DSC curves of neat PC18A and HCs (a) and their melting temperatures T_m and melting enthalpies ΔH_m (b) plotted against the number of carbon atoms. The ΔH_m value for dotriacontane is given as the sum of the three melting enthalpies at 46, 69, and 73C. (c) Melting temperatures of PC18A ($T_{m,PC18A}$) and HCs ($T_{m,HC}$) in PC18A/HC blends shown as a function of the weight fraction of HC (w_{HC}). HCs are *n*-tetradecane (circles), *n*-octadecane (triangle up), 1-docosanol (square), and *n*-dotriacontane (diamond).

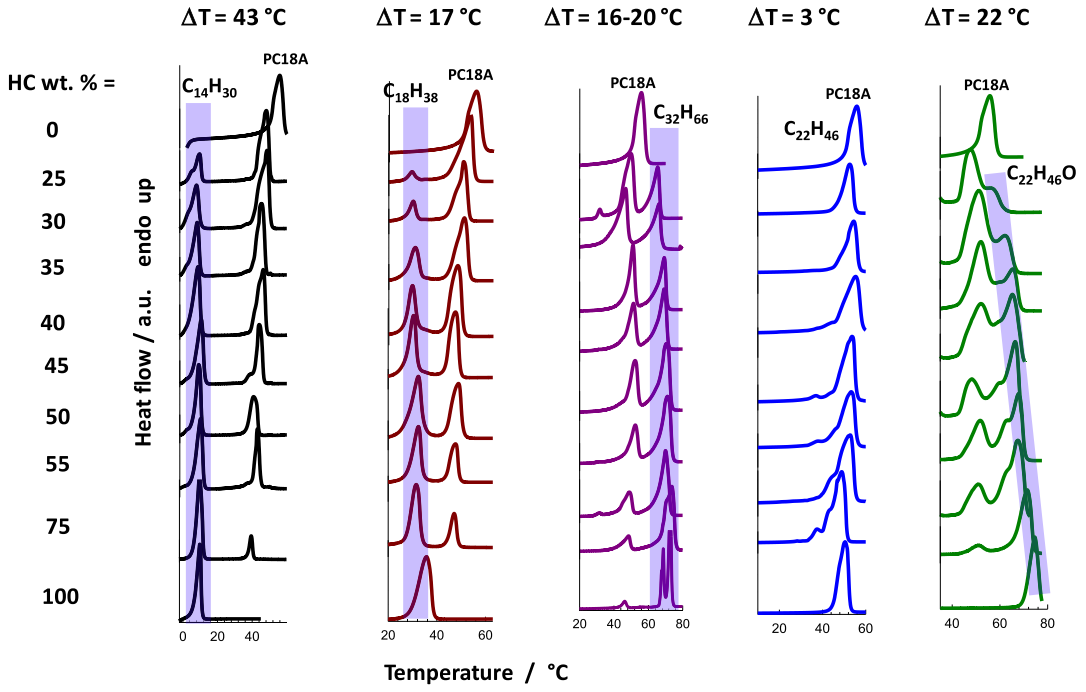

Figure 2. Heating DSC curves of dimer combinations of in situ-formed PC18A and HCs at various compositions. The temperature difference ΔT between the blend components and the weight percent of the hydrophobes are indicated.

melting enthalpy ΔH_m of HCs increases from 28.8 ± 0.4 to 105 ± 5 kJ·mol^{-1} with increasing chain length from 14 to 32 carbon atoms (Figure 1b). ΔH_m of PC18A is lower than that of $C_{18}H_{38}$ (33 ± 4 vs 62 ± 1 kJ·mol^{-1}), reflecting its lower degree of crystallinity. Considering that the melting enthalpy of crystalline C18A units is 71.2 kJ·mol^{-1},[30] around 46% of C18A units form side-chain crystals, with the rest being in the amorphous domains.

2.2. In Situ-Formed PC18A/HC Blends Constituting OHG Microinclusions. Assembling PC18A and HCs as functional and independent units into the microinclusions of an OHG is a challenging process because they can form eutectic mixtures and, hence, can show interfering phase transition behavior. Thus, avoiding the eutectic crystallization of PC18A and HCs is essential for realizing multishape-memory behavior and hence multistage switchable mechanical properties in OHGs. To mimic the microinclusions of OHGs,

https://doi.org/10.1021/acsami.4c12648
ACS Appl. Mater. Interfaces 2024, 16, 56146−56158

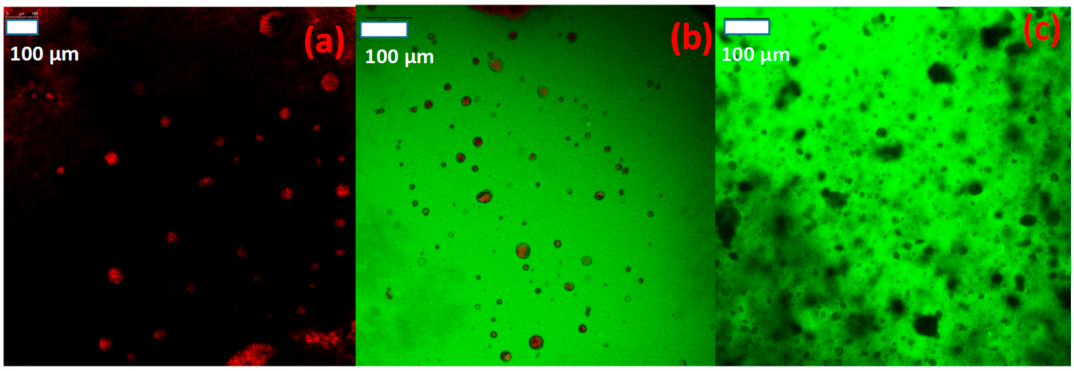

Figure 3. (a,b) CLSM images of the emulsion of C18A and $C_{18}H_{38}$ hydrophobes dispersed in an aqueous SF solution. SF = 6.5%. Ethanol = 17%. o/w = 5/5. In (a), the oil phase was stained with Nile red, while in (b), both the oil and the continuous aqueous phases were stained using Nile red and FITC, respectively. Scale bars: 100 μm. (c) CLSM image of the same emulsion after formation of the OHG. The continuous aqueous phase was stained using FITC. Scale bar: 100 μm.

the C18A monomer was photopolymerized in the presence of HCs and Irgacure photoinitiator to form PC18A/HC blends by varying the chain length and mass proportion of HCs. Figures 2 and S2a−e present heating and cooling DSC scans, respectively, of binary combinations of in situ-formed PC18A/HC blends at various compositions. The temperature difference ΔT between the blend components and the weight percentages of HCs in the blends are indicated in the figures. For PC18A/$C_{22}H_{46}$ blends with ΔT = 3 °C, the peaks of the blend components tend to merge into one broad transition, indicating cocrystallization, while all blends with $\Delta T \geq 16$ °C exhibit two endothermic and exothermic peaks, revealing that the individual blend components crystallize without substantial interference from the other blend component. Moreover, when the content of a particular component in the blend increases, the intensity of the peaks associated with that component also tends to increase. Figure 1c presents the melting temperatures of PC18A ($T_{m,PC18A}$) and HC components ($T_{m,HC}$) in the blends plotted against the weight fraction of HC (w_{HC}). The melting temperature for each blend component shifts to a slightly lower temperature upon dilution by the second component, suggesting some alteration in the crystal structure during blending. However, except for $C_{22}H_{46}O$, this effect is small with a maximum shift in T_m being of the order of 3−8 °C. A similar trend is observed in the T_{cry} and ΔH_m of the blend components (Figure S3).

Figure 2 also shows that the eutectic PC18A/$C_{22}H_{46}$ blends turn into noneutectic ones when $C_{22}H_{46}$ is substituted with the corresponding alcohol, $C_{22}H_{46}O$, due to increasing ΔT from 3 to 22 °C. However, PC18A/$C_{22}H_{46}O$ blends still exhibit enhanced cocrystallization, as evidenced by the broadening and partial merging of DSC peaks (Figures 2 and S2d). Previous works reveal that hydroxyl groups attached to alkanes promote cocrystallization with *n*-alkyl acrylates due to the cooperative hydrogen bonding, which exerts a significant effect on the structure of crystalline domains.[31] This is also supported by the significant shift in T_m of the $C_{22}H_{46}O$ component from 75 to 57 °C upon increasing the PC18A content of the blend, suggesting an alteration of the crystal formation (Figure 1c). Ternary combinations of PC18A/HC blends were also studied by DSC analysis to highlight the effect of the individual components on their crystallization behavior (Figures S4−S7). For instance, a PC18A/$C_{22}H_{46}$ binary blend exhibiting a single endothermic peak in DSC can be converted into a noneutectic blend with three distinct endothermic peaks when the amount of PC18A in the blend is reduced by adding $C_{18}H_{38}$ as the third component (Figure S4). A similar effect of PC18A was also observed by incorporating $C_{18}H_{38}$ into PC18A/$C_{22}H_{46}O$ binary blends (Figure S5). Formation of noneutectic mixtures by reducing the amount of PC18A in ternary blends is attributed to the 3D network structure of PC18A in the microinclusions. Thus, because HCs are dispersed in the PC18A network, the higher the amount of PC18A, the smaller the network mesh size, so that formation and growth of HC crystals are hindered at high PC18A contents.

Concluding this section, dual, triple, and quadruple combinations of in situ-formed PC18A, $C_{14}H_{30}$, $C_{18}H_{38}$, and $C_{32}H_{66}$ hydrophobes produce blends with multiple T_m's and T_{cry}'s, and hence, they are candidates as microinclusions of multiple-shape-memory OHGs. We should note that the experiments were also conducted using $C_{22}H_{46}O$ in combination with PC18A and $C_{18}H_{38}$ to form trimer blends in the microinclusions. No distinct peaks in DSC could be observed as compared to the above hydrophobes, and hence, the resulting OHGs containing $C_{22}H_{46}O$ exhibited weak temperature-dependent mechanical properties.

2.3. OHGs: Gel Fraction, Swelling Behavior, and Microstructure. OHGs were prepared by dispersing organic microinclusions containing C18A, HCs, and Irgacure in the continuous aqueous SF phase to produce a stable emulsion followed by UV polymerization at 23 ± 2 °C for 24. Figure 3a,b shows confocal laser scanning microscopy (CLSM) images of the emulsion system, where in (a), the dispersed microinclusion phase was stained with Nile red, while in (b), both the continuous aqueous and microinclusion phases were stained using fluorescein-5-isothiocyanate (FITC) and Nile red, respectively. The image of the same emulsion after the polymerization and hence after formation of the OHG is shown in Figure 3c, where the continuous aqueous phase was stained using FITC. It is seen that the individual hydrophobic domains are dispersed in the continuous hydrophilic phase. The emulsion system contains highly polydisperse droplets with diameters varying between 5 and 30 μm, while after polymerization, the diameters of the microinclusions remain almost unchanged. Thus, hydrophobic domains act as microinclusions in the OHG to provide shape-memory properties and thermomechanical performance.

The gel fraction W_g, which is the fraction of OHG precursors incorporated into the OHG structure, was

https://doi.org/10.1021/acsami.4c12648
ACS Appl. Mater. Interfaces 2024, 16, 56146−56158

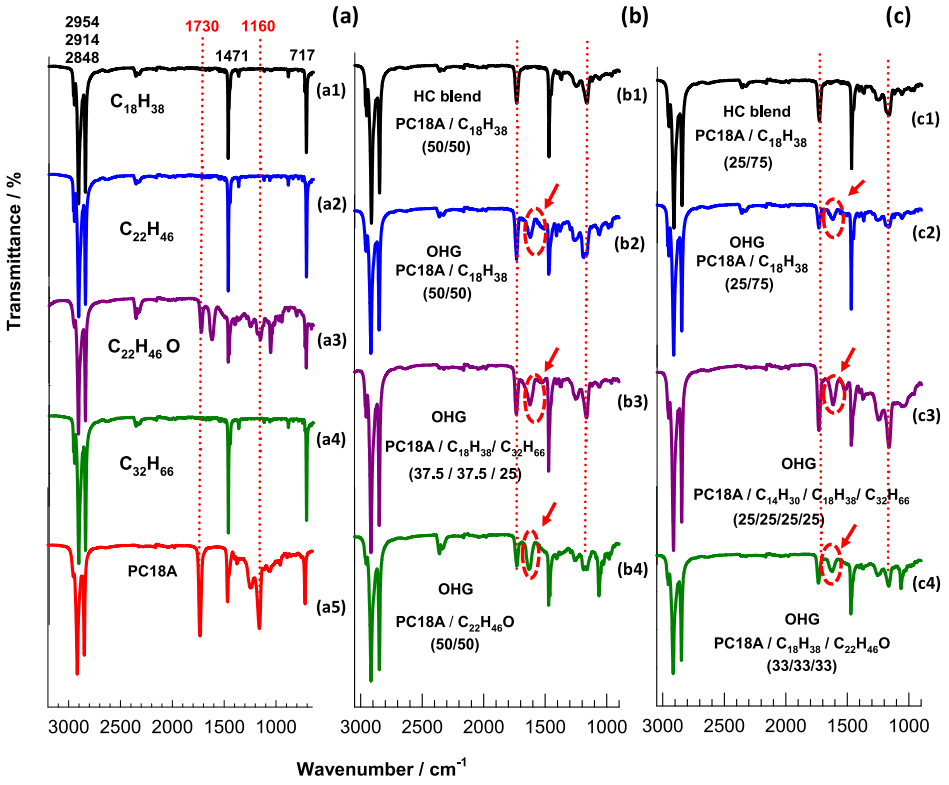

Figure 4. (a) FTIR spectra of the neat $C_{18}H_{38}$ (a1), $C_{22}H_{46}$ (a2), $C_{22}H_{46}$ O (a3), $C_{32}H_{66}$ (a4), and PC18A (a5) components of OHGs. (b,c) FTIR spectra of HC blends and OHGs. The spectra denoted by b1 and c1 represent PC18A/$C_{18}H_{38}$ blends with 50 and 75 wt % $C_{18}H_{38}$, respectively, while those denoted by b2 and c2 represent the corresponding OHGs. The spectra denoted by b3, c3, b4, and c4 represent OHGs containing PC18A/$C_{18}H_{38}$/$C_{32}H_{66}$, PC18A/$C_{14}H_{30}$/$C_{18}H_{38}$/$C_{32}H_{66}$, PC18A/$C_{22}H_{46}$ O, and PC18A/$C_{18}H_{38}$/$C_{22}H_{46}$ O blends, respectively. The compositions of the HC mixtures are indicated in parentheses.

determined by the extraction of the OHGs in a large amount of water. At PC18A weight fractions higher than 12.5% in the microinclusions, W_g of all OHGs was equal to unity, revealing that all their components are incorporated into the OHG networks (Table S1). The water content (EWC) of the OHGs in their swollen state is 51 ± 7%, which is the same as the water content just after the OHG synthesis. This nonswelling is in contrast to most hydrogels, where they swell significantly when immersed in water and hence considerably decrease their mechanical strength. The nonswelling behavior of OHGs is thus advantageous in many application areas including controlled network mesh size and hence controlled delivery of macromolecules.[32,33] At lower weight fractions of PC18A, W_g decreased to 0.75 ± 0.03, while EWC increased to 66−77%, indicating that the OHG components are partially dissolved in water and additional space for water is created within the OHG. This could be related to the formation of a loose physical network at low PC18A contents in the microinclusions facilitating the diffusion of HCs from the OHG to the water phase during extraction. Indeed, Young's modulus, i.e., the cross-link density of OHGs, was found to be directly related to their PC18A contents (see below).

The chemical structure of the OHGs was investigated by FTIR spectroscopy. Figure 4a shows the FTIR spectra of the neat $C_{18}H_{38}$ (a1), $C_{22}H_{46}$ (a2), $C_{22}H_{46}O$ (a3), $C_{32}H_{66}$ (a4), and PC18A (a5) components inside the microinclusions of the OHG. Five characteristic peaks are seen in all spectra, namely, C−H stretching vibrations of methylene and methyl groups appear at 2954, 2914, and 2848 cm^{-1}, the bending vibrations of the methyl groups, and in-plane rocking vibrations of the methylene groups appear at 1471 and 717 cm^{-1}, respectively. In the FTIR spectrum of PC18A, two additional sharp peaks appear at 1730 and 1160 cm^{-1} due to the stretching vibrations of C═O and C−O−C, respectively, as indicated by the vertical dotted lines in Figurer 4. All the peaks observed in the neat HCs and PC18A also appear in the spectra of both blends and OHGs, suggesting that no chemical reaction occurs between the components (Figure 4b,c). In addition, an extra peak at 1620 cm^{-1} is observable in the spectra of OHGs, as indicated by the red circles in Figure 4b,c. This peak, which is absent in the neat hydrophobic components and blends, is typical for the β-sheet structure of SF and indicates a conformational transition in SF from random coil to β-sheet structure and hence gelation in the continuous phase of OHGs.[34] Because the Amide-I region (1600−1700 cm^{-1}) is sensitive to the secondary structure of SF, the absorption peaks in this region are deconvoluted to separate the overlapping peaks at specific wavenumbers, namely, 1620, 1640, 1660, and 1698 cm^{-1}, corresponding to β-sheet, random coil, α-helix, and β-turn configurations, respectively.[34,35] A Gaussian model was applied to fit the separated peaks and quantify the contribution of each secondary structure to the overall spectrum (Figure S8). The β-sheet content of SF in aqueous solutions prior to gelation was 14 ± 2%, while after the formation of the OHG, it increases to 75 ± 5%. This significant increase in the β-sheet content is attributed to the rapid increase in the viscosity of SF solution after addition of the microinclusions, leading to fast gelation of the continuous SF phase and hence facilitating the formation of β-sheets. Moreover, the almost constancy of the β-sheet content of the OHGs reveals that the composition of

https://doi.org/10.1021/acsami.4c12648
ACS Appl. Mater. Interfaces 2024, 16, 56146−56158

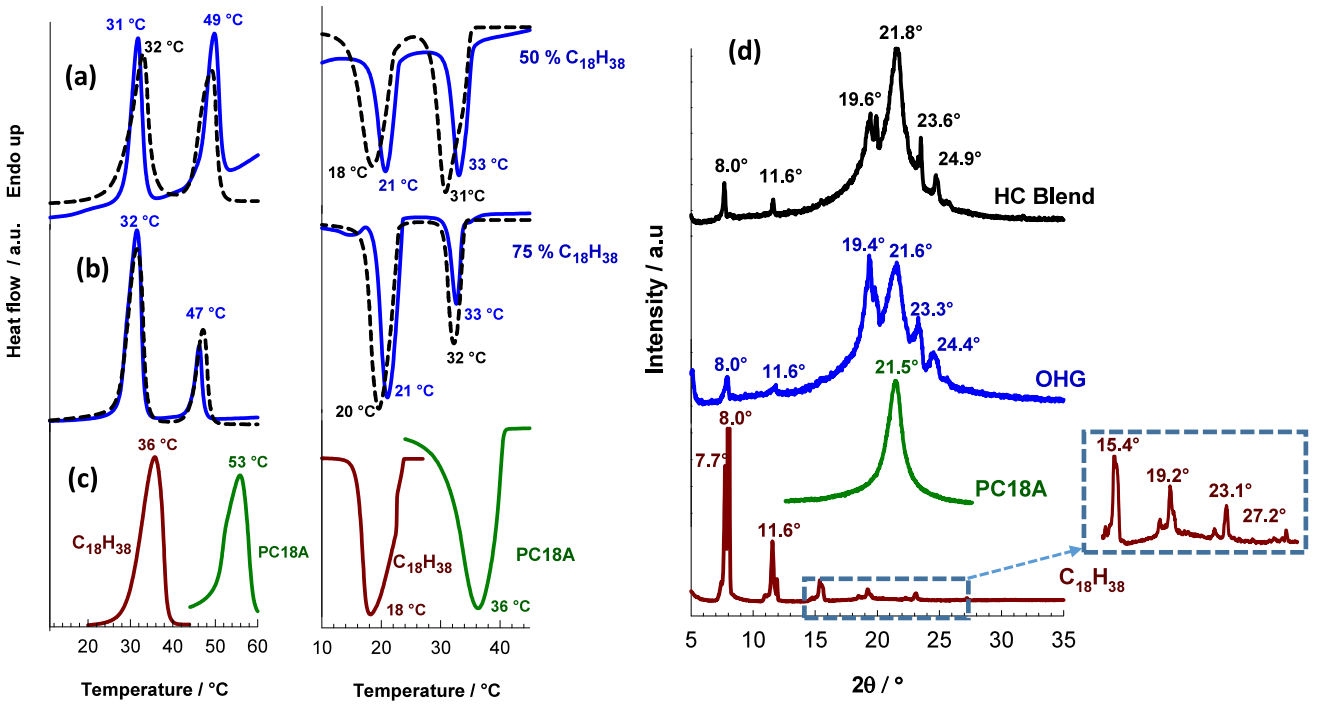

Figure 5. (a,b) DSC scans of HC blends containing PC18A and $C_{18}H_{38}$ (dashed curves) and corresponding OHGs (solid curves) during heating (left) and cooling steps (right). $C_{18}H_{38}$ = 50 (a) and 75 wt % (b). (c) DSC scans of the neat components. (d) X-ray diffraction patterns of the PC18A/$C_{18}H_{38}$ (75 wt %) blend, the corresponding OHG, and neat PC18A and $C_{18}H_{38}$ components.

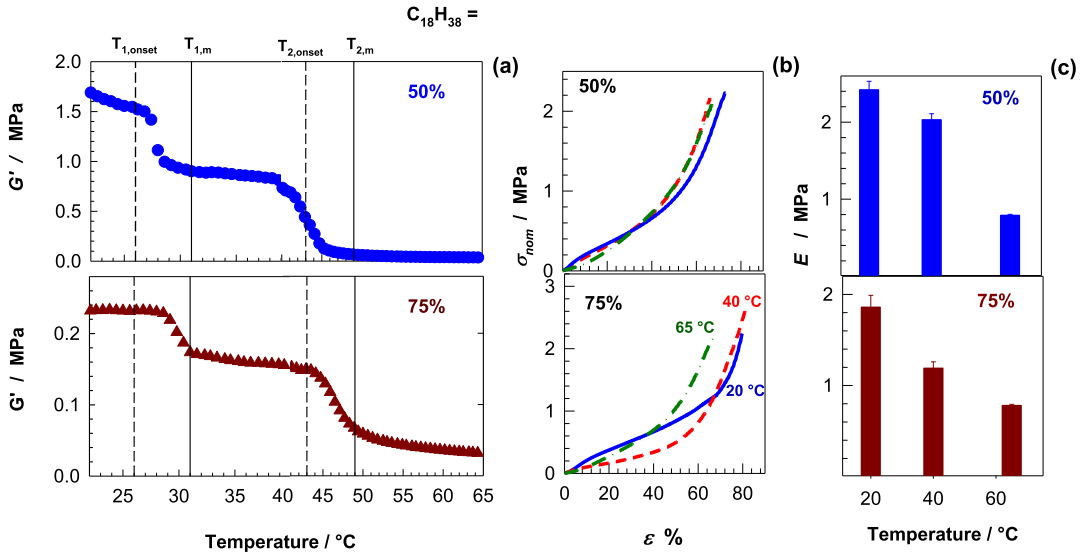

Figure 6. (a) Temperature dependence of the storage modulus G' of OHGs containing PC18A/$C_{18}H_{38}$ in the microinclusions with 50 and 75 wt % $C_{18}H_{38}$ as indicated. The onset and melting temperatures of OHGs are indicated by the vertical dashed and solid lines. (b,c) Stress−strain curves (b) and Young's modulus E (c) of the same OHGs at 20, 40, and 65 °C.

the microinclusions does not affect the morphology of SF in the continuous hydrogel phase of the OHGs.

2.4. OHGs with Dual, Triple, and Quadruple Combinations of PC18A/HCs in the Microinclusions. OHGs containing two hydrophobic components in their microinclusions were prepared using binary combinations of PC18A/$C_{18}H_{38}$ blends to create triple-shape-memory behavior. Figure 5a−c shows heating and cooling DSC scans of blends (dashed curves) and OHGs (solid curves) containing 50 (a) and 75 wt % $C_{18}H_{38}$ (b), together with the neat components (c). Both HC blends and OHGs exhibit two distinct peaks with T_m's and T_{cry}'s slightly shifting by a few degrees with respect to the neat PC18A and $C_{18}H_{38}$, reflecting independent crystallization of PC18A and $C_{18}H_{38}$ components. X-ray diffraction (XRD) patterns of the blend and the OHG with 75 wt % $C_{18}H_{38}$ together with the neat components are presented in Figure 5d. The neat PC18A exhibits a sharp peak at 21.5°, corresponding to a Bragg d-spacing of 0.41 nm, which is typical for hexagonal packing of octadecyl (C18) side chains.[36] This characteristic peak of PC18A is also observed in the diffraction patterns of both blend and OHG. For the neat $C_{18}H_{38}$, distinct characteristic diffraction peaks were observed

https://doi.org/10.1021/acsami.4c12648
ACS Appl. Mater. Interfaces 2024, 16, 56146−56158

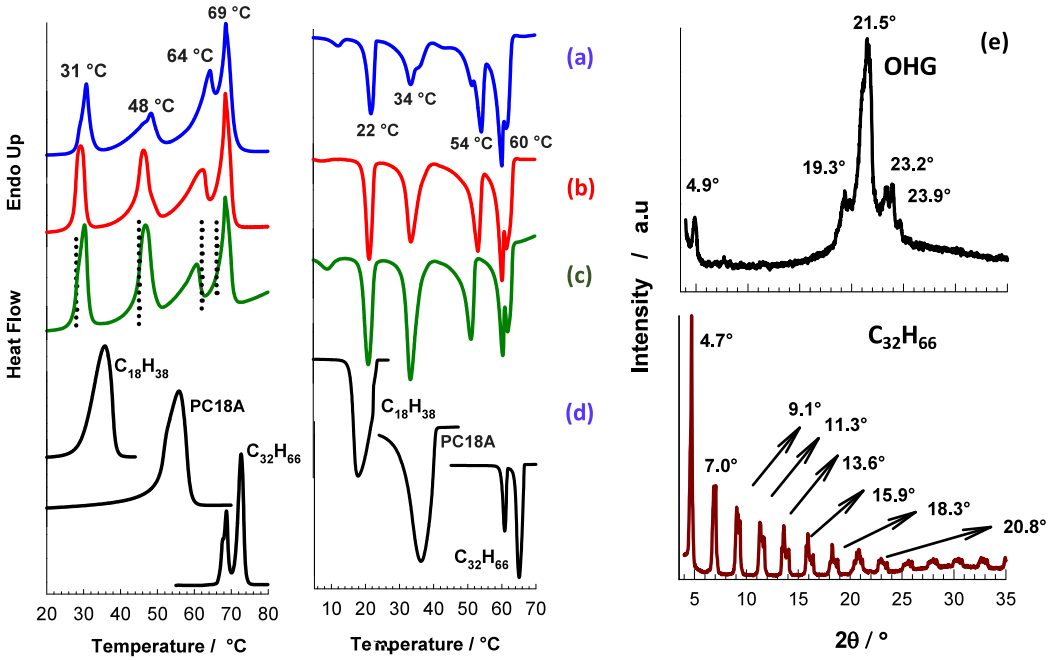

Figure 7. (a–d) DSC heating and cooling curves of OHGs based on PC18A/$C_{18}H_{38}$/$C_{32}H_{66}$ at weight ratios of 12.5/37.5/50 (a), 33.3/33.3/33.3 (b), and 37.5/37.5/25 (c), together with the neat components (d). The dotted vertical lines in (c) represent the shape recovery temperatures as indicated in Figure 8b. (e) XRD patterns of OHGs based on PC18A/$C_{18}H_{38}$/$C_{32}H_{66}$ at a weight ratio of 37.5/37.5/25 together with the neat $C_{32}H_{66}$.

at 2θ of 7.7, 8.0, 11.6, 15.4, 19.2, 23.1, and 27.2°. The most intense peaks of $C_{18}H_{38}$ between 7 and 12° significantly decrease upon incorporation into the blend and OHG, which is attributed to the dispersed state of the plate-like crystals in OHGs, which normally orient in powder specimen preparation.[37] In contrast, most of the weak reflections of $C_{18}H_{38}$ in the 2θ region between 19 and 27° become visible in both blend and OHG, as also observed in OHGs based on PC18A/$C_{18}H_{38}$/$C_{32}H_{66}$ blends (see below). Thus, most of the characteristic diffraction peaks of the pure components also appear in both blends and OHGs, although some of their values overlapped. This indicates that the crystal structure of the components did not change, as confined in the SF continuous phase, and the crystalline properties are well maintained.

The existence of two melting and crystallization peaks and separate crystalline domains in the OHGs resulted in a two-step change in their mechanical properties depending on temperature. Figure 6a shows the temperature dependence of the storage modulus G' of two OHG specimens containing 50 and 75 wt % $C_{18}H_{38}$ as indicated. The onset and melting temperatures of the OHGs as determined by DSC are indicated by the vertical dashed and solid lines, respectively. G' rapidly decreases at the transition temperatures due to the independent melting of $C_{18}H_{38}$ and C18A crystals, leading to a two-step decrease in G', i.e., in the cross-link density of the OHG. Figure 6b,c showing the stress–strain curves and Young's moduli E of OHGs reveals that the temperature significantly affects the initial slope of the stress–strain curves, i.e., Young's modulus E. The modulus E of the OHG with 50 wt % $C_{18}H_{38}$ is 2.4, 2.0, and 0.8 MPa at 20, 40, and 65 °C, i.e., below, between, and above its T_m's, respectively. Because PC18A forms the 3D network of the microinclusion phase while $C_{18}H_{38}$ remains trapped in it, the magnitude of E is determined by the amount of PC18A; i.e., at 20 °C, it increases from 1.9 ± 0.1 to 2.4 ± 0.1 MPa as the PC18A content is increased from 25 to 50 wt %.

OHGs were also designed using triple combinations of PC18A, $C_{18}H_{38}$, and $C_{32}H_{66}$ in their microinclusions. Figure 7a–d presents heating and cooling DSC scans of OHGs with PC18A, $C_{18}H_{38}$, and $C_{32}H_{66}$ at weight ratios of 12.5/37.5/50 (a), 33.3/33.3/33.3 (b), and 37.5/37.5/25 (c), together with the neat components (d). Four endothermic and exothermic peaks appear in the scans of the OHG's with T_m's shifting to lower temperatures by 3–5 °C as compared to the neat components (Figure 1). We should note that three of the DSC peaks are due to the separate melting and crystallization of the microinclusion components, while the fourth peak appearing at 64 and 54 °C during heating and cooling, respectively, is attributed to the transformation of $C_{32}H_{66}$ between orthorhombic and hexagonal phases. Figure 7e presents XRD patterns of OHGs containing PC18A/$C_{18}H_{38}$/$C_{32}H_{66}$ at a weight ratio of 37.5/37.5/25 together with the pure $C_{32}H_{66}$. In addition to the characteristic sharp peak of the PC18A component at 21.5° (d-spacing 0.41 nm) due to the crystalline C18 side chains, the peaks at 19.3, 23.2, and 23.9° in the XRD patterns of the OHG correspond to the $C_{18}H_{38}$ component (Figure 4d). The neat $C_{32}H_{66}$ shows strong diffraction peaks at 4.7, 7.0, 9.1, 11.3, 13.6, 15.9, 18.3, and 20.8° caused by its regular crystallization. The peak at 4.9° appearing in the OHG is attributed to the most intense peak of the $C_{32}H_{66}$ component. Thus, the peaks in the OHG reveal that each component retains its independent character and was not cocrystallized with each other.

Figure 8a shows the modulus E of the OHG specimens with various PC18A/$C_{18}H_{38}$/$C_{32}H_{66}$ weight ratios measured at 20, 40, 55, and 75 °C, i.e., below, between, and above the transition temperatures. Both the highest modulus and the largest extent of modulus change were observed for the OHG with the largest PC18A content of 37.5 wt %. This is expected

https://doi.org/10.1021/acsami.4c12648
ACS Appl. Mater. Interfaces 2024, 16, 56146–56158

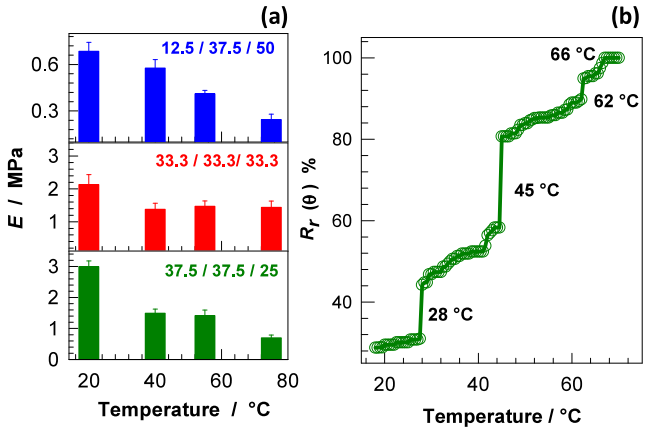

Figure 8. (a) Temperature dependence of Young's modulus E of OHGs based on PC18A/$C_{18}H_{38}$/$C_{32}H_{66}$ at various weight ratios as indicated. (b) Shape-recovery ratio R_r (θ) of an OHG specimen shown as a function of temperature. PC18A/$C_{18}H_{38}$/$C_{32}H_{66}$ weight ratio = 37.5/37.5/25.

due to the 3D network structure of PC18A, whose cross-link density increases with increasing amounts of PC18A content. E of this OHG around 4-fold changes (between 3.0 ± 0.2 and 0.7 ± 0.1 MPa) when the temperature is varied between below and above T_m's of the microinclusion components. A similar multistep change in the mechanical properties of the OHGs was also observed by performing temperature-sweep rheological measurements (Figure S9)

The existence of four-phase transition temperatures is reflected by the quintuple shape-memory effect in the OHGs, as demonstrated by the bending tests of OHG specimens immersed in water (Figure 9). The specimen in the permanent shape was first heated to 70 °C, which is above T_m's of the components. At this temperature, HCs in the OHG are in a liquid state, while semicrystalline PC18A becomes amorphous so that the specimen can easily be processed into a temporary shape. After deforming the specimen followed by cooling to 55 °C under strain, i.e., between T_m's of PC18A and $C_{32}H_{66}$, the first temporary shape was fixed (Figure 9). Deforming the specimen again at 55 °C followed by cooling to 40 °C, i.e., between T_m's of $C_{18}H_{38}$ and PC18A, the second temporary shape was fixed. Repeating these steps by deforming at 40 °C followed by cooling to 18 °C, i.e., below T_m's of the components, the third temporary shape was fixed. To recover the permanent shape, the specimen is reheated gradually at 70 °C, which provided stepwise melting of the crystalline domains and ensured that the chains returned to their entropically most favorable initial conformation. The shape-recovery behavior of an OHG specimen with a PC18A/$C_{18}H_{38}$/$C_{32}H_{66}$ weight ratio of 37.5/37.5/25 is presented in Figure 8b by the temperature-dependent shape-recovery ratio R_r (θ). The stepwise shape recovery occurs at 28, 45, 62, and 66 °C, i.e., at temperatures almost equal to the T_m's of the microinclusion components of the OHG specimen, as indicated by the vertical dotted lines in Figure 7c. Further heating above 70 °C results in a complete recovery of the original shape of the specimen.

A quintuple shape-memory effect was also observed in the OHGs containing four hydrophobic components in their microinclusions, namely, PC18A, $C_{14}H_{30}$, $C_{18}H_{38}$, and $C_{32}H_{66}$ with T_m's of 53 ± 2, 10, 36, and 73 °C, respectively. Figure 10a–c shows DSC scans of the OHGs with the four hydrophobes at various weight ratios. As compared to the neat hydrophobes, the T_m's of the hydrophobic components in the OHG significantly shift to smaller values, and the polymorphic phase-change temperature of $C_{32}H_{66}$ at 69 °C disappears, revealing their partial cocrystallization. However, four peaks in DSC scans over a wide range of temperatures, namely, between 6 and 58 °C and −0.4 and 48 °C during heating and cooling, respectively, were obtained, allowing

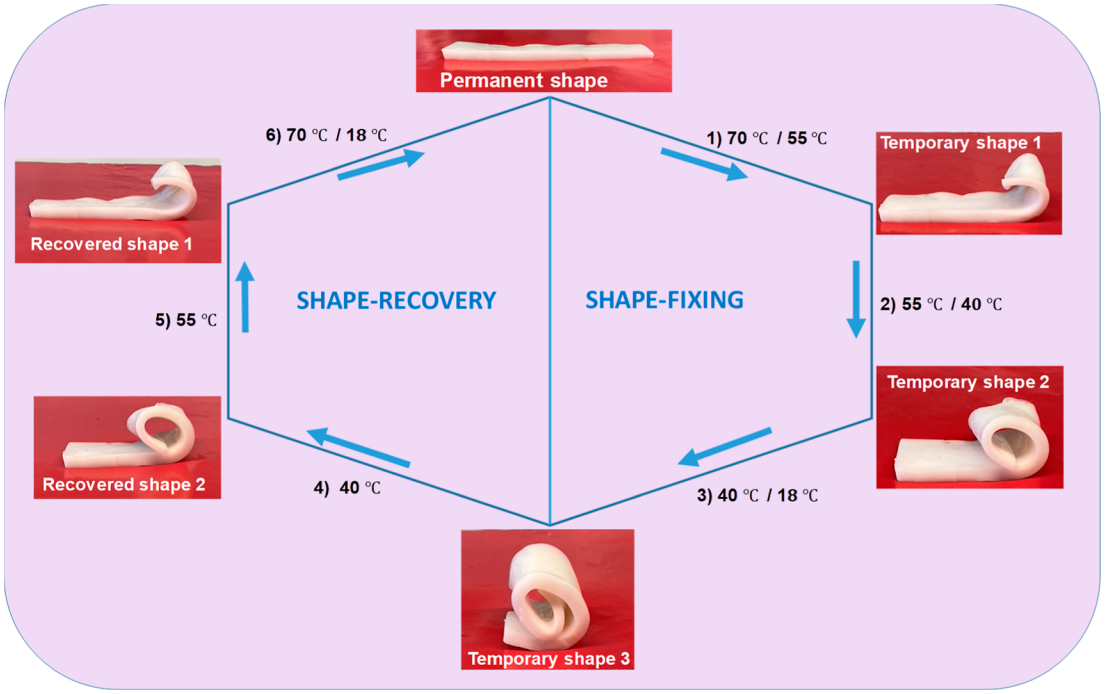

Figure 9. Quadruple shape-memory behavior of an OHG specimen containing triple combination of hydrophobes (PC18A/$C_{18}H_{38}$/$C_{32}H_{66}$ at a weight ratio of 37.5/37.5/25) in the oil phase.

https://doi.org/10.1021/acsami.4c12648
ACS Appl. Mater. Interfaces 2024, 16, 56146−56158

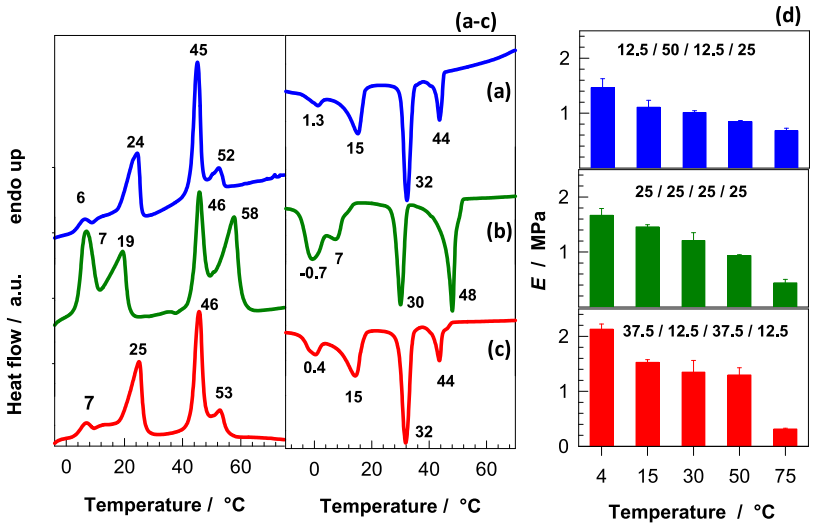

Figure 10. (a–c) DSC scans of OHGs based on PC18A/$C_{14}H_{30}$/$C_{18}H_{38}$/$C_{32}H_{66}$ at weight ratios 12.5/50/12.5/25 (a), 25/25/25/25 (b), and 37.5/12.5/37.5/12.5 (c). (d) Temperature-dependent Young's modulus E of the same OHGs at various weight ratios as indicated.

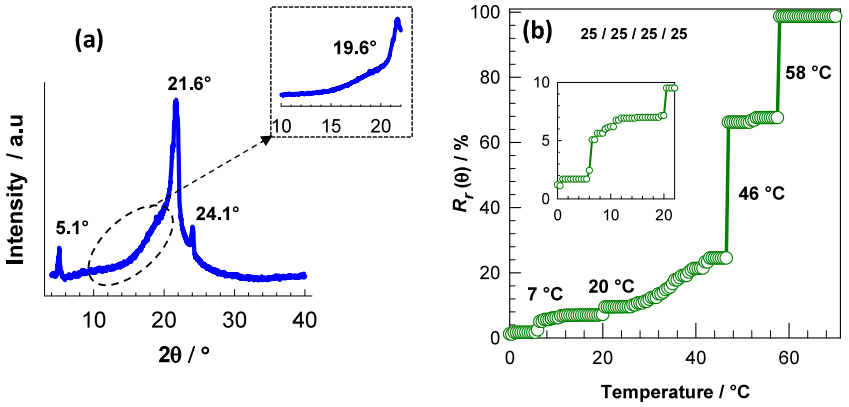

Figure 11. (a) X-ray diffraction patterns of OHGs based on PC18A/$C_{14}H_{30}$/$C_{18}H_{38}$/$C_{32}H_{66}$ at equal weight ratios. (b) Shape-recovery ratio R_r (θ) of an OHG specimen shown as a function of temperature. PC18A/$C_{18}H_{38}$/$C_{32}H_{66}$ weight ratio as indicated.

mechanical property variation over a wide range. Figure 11a presents the XRD patterns of the OHG with equal amounts of PC18A/$C_{14}H_{30}$/$C_{18}H_{38}$/$C_{32}H_{66}$ components. In addition to the characteristic sharp peak of PC18A at 21.6° (d-spacing 0.41 nm), the peaks at 5.1 and 24.1° are due to the $C_{32}H_{66}$ and $C_{18}H_{38}$ components of the OHG, respectively. Moreover, because $C_{14}H_{30}$ is a liquid at room temperature, which strongly absorbed X-rays and inhibited diffraction, only a flat peak characterizing $C_{14}H_{30}$ is observed at 19.6° (inset in Figure 11a).

Figure 10d shows temperature-dependent variation of the modulus E of OHG specimens with various PC18A/$C_{14}H_{30}$/$C_{18}H_{38}$/$C_{32}H_{66}$ weight ratios. Five distinct modulus plateaus are observed over a wide range of temperatures, e.g., 4, 15, 30, 50, and 75 °C, i.e., at below, between, and above T_m's of the components. The highest modulus and the largest extent of modulus change were observed for the OHG with the largest PC18A content of 37.5 wt %. The modulus E of this OHG around 7-fold changes (between 2.1 ± 0.1 and 0.31 ± 0.01 MPa) when the temperature is varied between below and above Tm's of the microinclusion components. Figure 11b shows the temperature-dependent shape-recovery ratio R_r (θ) of an OHG specimen with equal amounts of PC18A/$C_{14}H_{30}$/$C_{18}H_{38}$/$C_{32}H_{66}$. The stepwise shape recovery occurs at 7, 20, 46, and 58 °C, which are equal to the melting temperatures of the hydrophobic components in the OHG (Figure 10b). Thus, a multishape-memory effect in OHGs with discrete transitions could be created using noneutectic mixtures of HCs trapped in a semicrystalline PC18A micronetwork with a wide range of adjustable temperatures.

In addition to the multiple-shape-memory behavior of the OHGs, the coexistence of their opposing components provided several additional functionalities such as freeze tolerance and hence stretchability and elasticity at subzero temperatures. Because of the existence of SF, PDMAA, and BAAm in the continuous hydrogel phase of OHG, the freezing temperature T_{cry} of the hydrogel phase as well as OHGs was reduced to −15 ± 2 °C, which provided them with self-antifreeze and elastic properties up to this temperature (Figure 12a). In order to further increase the range of the unfrozen regime, glycerol was used, which is known to reduce the water freezing point due to strong H-bonds between glycerol and water disrupting ice crystals at low temperatures.[38,39] It was found that immersing the OHG specimens in glycerol to form a layer on the surface of the material prevented them from freezing up to at least −60 °C, and they exhibited elastic behavior even at very low temperatures (Figure 12b). Moreover, the freeze resistance was independent of the type

https://doi.org/10.1021/acsami.4c12648
ACS Appl. Mater. Interfaces 2024, 16, 56146−56158

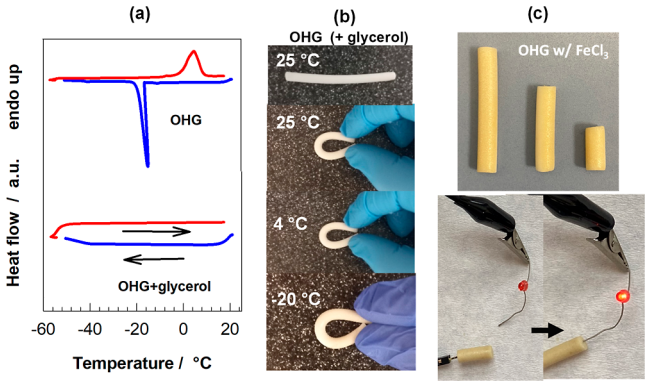

Figure 12. (a) DSC scans of the OHG with and without glycerol during cooling (blue curve) and heating (red curve) between 20 and −60 °C at a rate of 5 °C·min^{-1}. The second heating and cooling cycle is shown in the figure. (b) Deformation of an OHG specimen coated with glycerol at various temperatures as indicated. OHG contains PC18A/$C_{18}H_{38}$/$C_{32}H_{66}$ at a weight ratio of 37.5/37.5/25 in the microinclusions. (c) OHG specimens containing 10 μL of 8 wt % ferric chloride hexahydrate per 5 mL of the aqueous phase of the OHG precursor and their conductive behavior. Synthesis conditions of the OHG are given in Table S9 as OHG-8.

of OHGs due to the constant concentration and composition of the solutes in the continuous hydrogel phase of the OHGs (see Materials and Methods section).

Multishape-memory OHGs also exhibited conductivity when a small amount of Fe^{3+} ions was included in the continuous hydrogel phase. Because the hydrogel phase of the OHG contains 50 wt % water (Table S1), the free Fe^{3+} ions dissolved in this phase are mobile throughout the gel, so the ionic conductivity is attributed to the mobile Fe^{3+} ions within the hydrogel. We should mention that the amount of Fe^{3+} ions as well as the exposure time of Fe^{3+} on SF affected the aqueous phase properties during gelation. For instance, the aqueous phase immediately turned into a gel phase after addition of >100 μL of 8 wt % $FeCl_3.6H_20$ into 5 mL of the aqueous phase due to the complex formation between SF and Fe^{3+}. To prevent gelation, 10 μL of 8 wt % $FeCl_3.6H_20$ was added at the end of the stirring time (1 h) and just prior to the addition of the oil phase.

To demonstrate the conductivity of the developed OHGs, we used a light-emitting diode (LED) in the circuit to power it up using the OHG specimens with different lengths. The OHGs were placed in the circuit as shown in Figure 12c. Furthermore, the circuit was powered up using an external power supply connected to both ends of the LED through the OHG, leading to LED light. This experiment showed that dissolution of 10 μL of 8 wt % ferric chloride hexahydrate ($FeCl_3{\cdot}6H_2O$) in 5 mL of the aqueous phase of the OHG precursor leads to the formation of OHGs with a conductivity of 1.204 S/m (Figure 12c).

3. CONCLUSIONS

The ability of the OHGs to mimic the synergistic biphasic nature of biological systems offers a promising avenue for developing advanced materials with unique properties. We presented here a simple and inexpensive approach to fabricate SF-based OHGs with multistage switching mechanics by incorporating several long-chain saturated hydrocarbons (HCs) into the semicrystalline PC18A microinclusions as independent functional units. By changing the chain length and mass proportion of HCs, a series of OHGs with tunable transition temperatures could be obtained, meeting various applications. The HCs and PC18A in the microinclusions of the OHG melt and crystallize at their own phase transition temperatures and create stepwise switching viscoelastic and mechanical properties. The continuous hydrophilic phase of the OHG precursor consists of an aqueous SF solution, while the hydrophobic droplet phase consists of the C18A monomer and HCs with various chain lengths between 14 and 32 carbon atoms, namely, *n*-tetradecane, *n*-octadecane, *n*-docosane, *n*-dotriacontane, and 1-docosanol. After addition of the C18A/HC mixture containing Irgacure photoinitiator into the continuous aqueous SF phase under stirring, a stable oil-in-water emulsion was obtained, which was then photopolymerized at 23 ± 2 °C to obtain nonswelling OHGs with multiple-shape-memory behavior. The phase transition and shape-recovery temperature of the OHGs could be adjusted over a wide range by changing the type and amount of HCs. Young's modulus of OHGs up to 7-fold changes (between 2.1 ± 0.1 and 0.31 ± 0.01 MPa) when the temperature is varied between below and above T_m's of the microinclusion component. A similar multistep change in the mechanical properties of the OHGs was also observed by performing temperature-sweep rheological measurements. The mechanical properties of OHGs are not affected by the chain length of HCs, but they are affected by the amount of PC18A in the microinclusions, as demonstrated in Figures 6c, 8a, and 10d showing increasing Young's modulus of OHGs with increasing PC18A content. This is attributed to the 3D network structure of PC18A in the microinclusions. Thus, because HCs are dispersed in the PC18A network, the higher the amount of PC18A, the smaller the network mesh size, so that the modulus increases with PC18A content. The multishape-memory effect is an advanced capability in some shape-memory hydrogels, where these hydrogels can remember and revert to multiple distinct shapes upon exposure to specific stimuli such as temperature. OHGs containing two, three, or four hydrophobic components in their microinclusions were prepared to create triple- and quintuple-shape-memory behavior. The multishape-memory effect appears in OHGs because of the existence of different crystalline domains having different thermal properties. Thus, the OHGs become mobile or rigid at different temperatures so that the crystalline domains can lock in different shapes at different temperatures. The results thus presented reveal that incorporation of multiple crystalline phases using HCs exhibiting a wide range of phase transition temperatures creates OHGs with switchable mechanics and multiple-shape-memory behavior. The presence of hydrophilic and hydrophobic phases in the OHG grants additional features such as conductivity and freeze tolerance.

4. MATERIALS AND METHODS

4.1. Materials. *Bombyx mori* silkworm cocoons (Kozabirlik, Agriculture Sales Cooperative for Silk Cocoon, Bursa, Turkey), sodium carbonate (Na_2CO_3, Merck, 99.9%), lithium bromide (LiBr, Merck, 99%), polyethylene glycol (PEG-10000, Sigma-Aldrich, 10,000 g·mol^{-1}), ethanol (Merck, ≥99.9%), *N*,*N*′-methylenebis-(acrylamide) (BAAm, Sigma-Aldrich, 99%), *n*-octadecyl acrylate (C18A, Sigma-Aldrich, 97%), 2-hydroxy-4′-(2-hydroxyethoxy)-2-methylpropiophenone (Irgacure 2959, Sigma-Aldrich, St. Louis, MO), and *N*,*N*-dimethylacrylamide (DMAA, Sigma-Aldrich, 99%) were used as received. The HCs *n*-tetradecane ($C_{14}H_{30}$, Merck, 99%), *n*-octadecane ($C_{18}H_{38}$, Merck, 99%), *n*-docosane ($C_{22}H_{46}$, Merck, 99%), *n*-dotriacontane ($C_{32}H_{66}$, Merck, 99%), and 1-docosanol

https://doi.org/10.1021/acsami.4c12648
ACS Appl. Mater. Interfaces 2024, 16, 56146−56158

($C_{22}H_{46}O$, Merck, 97%) were used as received. Nile red (Sigma-Aldrich) and fluorescein isothiocyanate isomer I (FITC, Sigma-Aldrich, ≥90%) were used for staining and visualizing different parts of the OHGs.

4.2. Isolation and Preparation of SF.[34] About 10 g of *Bombyx mori* silkworm cocoons was cut into small pieces. After being washed with distilled water, the cocoon pieces were boiled in a 0.02 M Na_2CO_3 solution (1 L) for 1 h. This step is crucial for removing sericin, the glue-like protein that surrounds the fibroin fibers in the cocoon, ensuring that only pure fibroin is left. The degummed SF was then washed five times with 1 L of distilled water at 70 °C for 20 min each to remove any residual sericin and Na_2CO_3. The washed SF was dried at room temperature for 2 days. Seven g of the dried SF was dissolved in 35 mL of a 9.3 M LiBr solution at 60 °C for 2 h. LiBr effectively dissolves the SF by breaking down its crystalline structure, making it soluble. The SF solution was then dialyzed against water using a 10,000 MWCO dialysis tubing (Snake Skin, Pierce) for 3 days. The water was changed three times a day to ensure complete removal of LiBr. After dialysis, the solution was centrifuged to remove any undissolved particles, ensuring a homogeneous SF solution. The final SF concentration was found to be approximately 5 wt %. This was determined by weighing the remaining solid after drying a known volume of the SF solution. To prepare SF solutions with higher concentrations, the 5 wt % SF solution was further concentrated by dialysis against aqueous solutions of 15 w/v % PEG-10000 using 3500 MWCO dialysis tubing. PEG acts as an osmotic agent, drawing water out of the SF solution and thereby increasing the concentration of SF. All SF solutions were stored at 4 °C to prevent microbial growth and degradation. The solutions were used within 2 weeks to ensure freshness and consistency in experimental conditions. A stock solution with a concentration of 9.51 w/v % SF was prepared and used for subsequent experiments.

4.3. Preparation of PC18A/HC Blends. To determine the conditions for the formation of noneutectic PC18A/HC mixtures, the C18A monomer and HCs containing Irgacure 2959 (0.2 mol % with respect to C18A) were mixed at various compositions. The polymerization of C18A was then conducted under UV light at 23 ± 2 °C for 24 h. PC18A/HC blends thus obtained were subjected to DSC and XRD measurements, as detailed below. Synthesis conditions of blends at various compositions are listed in Tables S2−S6.

4.4. Synthesis of OHGs. The aqueous phase of the OHG precursors was prepared by dissolving DMAA, BAAm, and Irgacure 2959 at 40 °C in an aqueous stock SF solution containing ethanol. Throughout this study, the subsequent parameters were maintained as they were the most effective means of achieving a stable emulsion of hydrophobic droplets measuring 12 ± 4 μm in diameter:[25] SF = 6.5 w/v %; oil-to-water volume ratio = 1:1. DMAA = 7.5 w/w. Ethanol = 17 vol %. BAAm and Irgacure 2959 = 1 and 0.2 mol %, respectively, with respect to DMAA. The oil phase consisted of the C18A monomer and HCs at various combinations and Irgacure 2959 (0.2 mol % of C18A). The oil phase was gradually added to the aqueous phase drop by drop while being continuously stirred for 5 min at 40 °C and 1400 rpm. We should note that, because the T_m of *n*-dotriacontane is higher than that of the other HCs, the temperature of the oil phase was adjusted to 65 °C to facilitate its solubility. The milky white emulsion was then transferred into plastic syringes of 1 and 50 mL in volumes, and they were placed into the UV reactor at 23 ± 2 °C for 24 h. Synthesis conditions of OHGs at various compositions are listed in Tables S7−S10. Typically, to prepare the OHGs containing equal amounts of C18A and *n*-octadecane in the microinclusions, 3.42 mL of aqueous SF stock solution and 0.36 mL of distilled water were mixed, and 0.84 mL of ethanol was dropwise added to this solution. After stirring the aqueous phase for 1 h at 40 °C and 100 rpm, DMAA (0.39 mL), BAAm (5.83 mg), and Irgacure 2959 (1.69 mg) were added. After 1 h of stirring time, the oil phase consisting of C18A (2.0 g) containing Irgacure 2959 (2.8 mg) and *n*-octadecane (2.0 g) was dropwise added to the aqueous phase while being continuously stirred for 5 min at 40 °C and 1400 rpm. The UV polymerization was then conducted at 23 ± 2 °C for 24 h. After polymerization, the OHG specimens were placed in an excess of water for 3−4 days by replacing water every day to remove the soluble species and to attain the swelling equilibrium. A part of the OHG specimens was dried in a vacuum oven (Nucleus, NVE) at 37 °C for 3−4 days to determine the gel fraction and swelling ratio. All other measurements, including rheological, mechanical, DSC, and shape-memory tests, were conducted on the OHGs in their equilibrium swollen states in water.

4.5. Characterization. Attenuated total reflectance Fourier transform infrared (ATR-FTIR) spectroscopy observations on an Agilent Technologies Cary 630 ATR-FTIR spectrophotometer were used to determine the secondary structure of SF. The Amide-I region of the spectra (typically 1600−1700 cm^{-1}), which is sensitive to the protein's secondary structure, was deconvolved using a Gaussian model after applying a linear baseline correction. This was done using PeakFit software (Version 4.12, SeaSolve Software Inc.). Specific band positions at 1620, 1640, 1660, and 1698 cm^{-1} corresponding to the β-sheet, random coil, α-helix, and β-turn conformations of SF, respectively, were fixed during the curve fitting process by allowing the widths and heights to vary (Figure S3). Differential scanning calorimetry (DSC) measurements were conducted on a PerkinElmer DSC 4000 instrument under a nitrogen atmosphere. Approximately 10 mg of each specimen was weighed and sealed in aluminum pans. The samples were then scanned over a temperature range from 0 to 65 °C. Melting enthalpies ΔH_m were calculated from the area under the endothermic peaks in the DSC curves. The degree of crystallinity f_{cry}, which is the fraction of C18A units forming crystalline domains, was calculated as reported before.[36] X-ray diffraction (XRD) measurements were performed on dried specimens on a PANalytical X-Pert PRO multipurpose diffractometer using Ni-filtered CuKα radiation with a wavelength (λ) of 0.15418 nm at 45 kV and 40 mA in a 2θ range of 5−40°. Confocal laser scanning microscopy (CLSM, Leica TCs-SPE, Japan) was employed to visualize the distinct hydrogel and organogel components of the OHGs. FITC and Nile red were used to stain the hydrogel and organogel components of the OHGs, respectively. The ionic conductivity of the OHGs was measured using an impedance analyzer (Zurich Instruments MFIA Impedance Analyzer). The impedance was obtained using this method, which yielded a complex value containing real and imaginary parts. The real part of the impedance represents the resistance (R) of the OHGs. Furthermore, the conductivity of the OHGs was calculated using the equations

$$\text{resistance} = RL/A \tag{1}$$

$$R = 1/C \tag{2}$$

where R, L, A, and C are resistivity, length, area, and conductance, respectively. The equilibrium water content EWC of the OHGs was calculated as EWC = $1-1/q_w$, where q_w is the equilibrium weight swelling ratio of the OHGs with respect to the dry state. Moreover, the gel fraction W_g was calculated using the equation

$$W_g = \frac{m_{dry}}{m_o C_o} \tag{3}$$

where m_o is the mass of OHG after preparation and C_o is the concentration of SF, DMAA, BAAm, C18A, and HCs in the emulsion system.

Rheological tests were conducted with a Bohlin Gemini 150 rheometer equipped with a Peltier device to precisely control the temperature. A parallel plate geometry with a diameter of 20 mm and a water trap to prevent the evaporation of water from samples were used. Water-swollen OHG specimens prepared in 20 mL plastic syringes with an internal diameter of 20 mm were used for the measurements. Frequency (ω) sweep tests were carried out at a strain γ_o of 0.1%. The modulus (G') dependence of OHGs on temperature was investigated by heating the OHG specimens from 25 to 65 °C at a rate of 4 °C·min^{-1} at γ_o = 0.1% and ω = 6.28 rad·s^{-1}.

Mechanical properties of water-swollen OHGs were characterized at 23 ± 2 °C using a Zwick-Roell universal test machine equipped with a load cell of 500 N. The tests were performed with a 0.05 N preload at a speed of 5 mm·min^{-1} in order to guarantee full contact

https://doi.org/10.1021/acsami.4c12648
ACS Appl. Mater. Interfaces 2024, 16, 56146−56158

between the sample and the surface. Young's modulus E was calculated based on stress−strain curves between 2 and 4% compression. The nominal stress value σ_{nom}, which is the force per cross-sectional area of an undeformed specimen, was used to represent stress, and ε, which is the sample length change with respect to its starting length, was used to represent strain.

Bending tests were used to determine the OHGs' shape-memory efficiency. OHG specimens measuring 85 × 20 × 2 mm were subjected to heat treatment up to 65 °C and then deformed to a bent shape with a distorted angle of Θ_d. After that, they spent 5 min at 25 °C to fix this temporary shape while under stress. The specimens' fixed angles (Θ_f) were measured after unloading in order to calculate the shape fixity ratios (R_f) of OHGs. In the end, the OHG specimens were heated progressively from 25 to 70 °C. Recovery angles Θ_r were measured at temperature intervals of 1−3 °C, and recovery ratios R_r were computed. R_f and R_r of OHGs were calculated as

$$R_f = \frac{\theta_f - 180}{\theta_d - 180} \quad (4)$$

$$R_r = \frac{\theta_d - \theta_r}{\theta_d - 180} \quad (5)$$

where Θ_d, Θ_f, and Θ_r are the deformed angle under load, fixed angle after unloading, and recovered angle upon heating, respectively. The shape-fixity ratio R_f of OHGs based on PC18A, $C_{18}H_{38}$, and C_{32}/H_{66} was 71 ± 2%, while R_f increased to 99% for OHGs containing four hydrophobic components, namely, PC18A/$C_{14}H_{30}$/$C_{18}H_{38}$/C_{32}/H_{66}.

■ ASSOCIATED CONTENT

Supporting Information

The Supporting Information is available free of charge at https://pubs.acs.org/doi/10.1021/acsami.4c12648.

Additional experimental details, DSC curves, FTIR spectra, and rheological data (PDF)

■ AUTHOR INFORMATION

Corresponding Author

Oguz Okay − *Department of Chemistry, Istanbul Technical University, Maslak, Istanbul 34469, Turkey;* orcid.org/0000-0003-2717-4150; Phone: +90 212 285 3156; Email: okayo@itu.edu.tr

Authors

Cigdem Buse Oral − *Department of Chemistry, Istanbul Technical University, Maslak, Istanbul 34469, Turkey*

Esra Su − *Faculty of Aquatic Sciences, Istanbul University, Fatih, Istanbul 34134, Turkey*

Complete contact information is available at: https://pubs.acs.org/10.1021/acsami.4c12648

Author Contributions

The manuscript was written through contributions of all authors. All authors have given approval to the final version of the manuscript.

Funding

This work was supported by the Scientific and Technical Research Council of Turkey (TUBITAK) 1001, project no. 121Z568. O.O. thanks the Turkish Academy of Sciences (TUBA) for the partial support.

Notes

The authors declare no competing financial interest.

■ REFERENCES

(1) Huang, J.; Fang, R.; Zhao, T.; Liu, M. Bioinspired Functional Organohydrogels with Synergistic Multiphases Heterostructure. *Polymer* **2020**, *190*, 122214.

(2) Mo, J.; Prévost, S. F.; Blowes, L. M.; Egertová, M.; Terrill, N. J.; Wang, W.; Elphick, M. R.; Gupta, H. S. Interfibrillar Stiffening of Echinoderm Mutable Collagenous Tissue Demonstrated at the Nanoscale. *Proc. Natl. Acad. Sci. U.S.A.* **2016**, *113*, E6362−E6371.

(3) Yang, Y.; Liu, Q.; Zhao, T.; Ru, Y.; Fang, R.; Xu, Y.; Huang, J.; Liu, M. Magnetic-Programmable Organohydrogels with Reconfigurable Network for Mechanical Homeostasis. *Nano Res.* **2021**, *14*, 255−259.

(4) Zhang, Z.; Hao, J. Bioinspired Organohydrogels with Heterostructures: Fabrications, Performances, and Applications. *Adv. Colloid Interface Sci.* **2021**, *292*, 102408.

(5) Le, X.; Shang, H.; Chen, T. A. A Short Review on Organohydrogels: Constructions and Applications. *Macromol. Chem. Phys.* **2024**, *225*, 2300377.

(6) Zhuo, S.; Zhao, Z.; Xie, Z.; Hao, Y.; Xu, Y.; Zhao, T.; Li, H.; Knubben, E. M.; Wen, L.; Jiang, L.; Liu, M. Complex Multiphase Organohydrogels with Programmable Mechanics Toward Adaptive Soft-Matter Machines. *Sci. Adv.* **2020**, *6* (5), No. eaax1464.

(7) Storey, K. B.; Storey, J. M. Molecular Biology of Freezing Tolerance. *Compr. Physiol.* **2013**, *3*, 1283−1308.

(8) Xu, Y.; Rong, Q.; Zhao, T.; Liu, M. Anti-Freezing Multiphase Gel Materials: Bioinspired Design Strategies and Applications. *Giant* **2020**, *2*, 100014.

(9) Lan, J.; Shi, L.; Xiao, W.; Zhang, X.; Wang, S. A. A Rapid Self-Pumping Organohydrogel Dressing with Hydrophilic Fractal Microchannels to Promote Burn Wound Healing. *Adv. Mater.* **2023**, *35*, 2301765.

(10) Hou, J.; Zhang, X.; Wu, Y.; Jie, J.; Wang, Z.; Chen, G.-Q.; Sun, J.; Wu, L.-P. Amphiphilic and Fatigue-Resistant Organohydrogels for Small-Diameter Vascular Grafts. *Sci. Adv.* **2022**, *8*, No. eabn5360.

(11) Wu, Z.; Yang, X.; Wu, J. Conductive Hydrogel- and Organohydrogel-Based Stretchable Sensors. *ACS Appl. Mater. Interfaces* **2021**, *13*, 2128−2144.

(12) Xu, X.; Wan, X.; Li, H.; Zhang, Y.; He, W.; Wang, S.; Wang, M.; Hou, X.; Wang, S. Oil-Polluted Water Purification via the Carbon-Nanotubes-Doped Organohydrogel Platform. *Nano Res.* **2022**, *15*, 5653−5662.

(13) Ding, Q.; Wu, Z.; Tao, K.; Wei, Y.; Wang, W.; Yang, B. R.; Xie, X.; Wu, J. Environment Tolerant, Adaptable and Stretchable Organohydrogels: Preparation, Optimization, and Applications. *Mater. Horiz.* **2022**, *9*, 1356−1386.

(14) Zhang, Q.; Hua, W.; Feng, J. A. A Facile Strategy to Fabricate Multishape Memory Polymers with Controllable Mechanical Properties. *Macromol. Rapid Commun.* **2016**, *37*, 1262−1267.

(15) Zhu, C.-N.; Bai, T.; Wang, H.; Ling, J.; Huang, F.; Hong, W.; Zheng, Q.; Wu, Z.-L. Dual-Encryption in a Shape-Memory Hydrogel with Tunable Fluorescence and Reconfigurable Architecture. *Adv. Mater.* **2021**, *33*, 2102023.

(16) Wang, Y. J.; Zhang, X. N.; Song, Y.; Zhao, Y.; Chen, L.; Su, F.; Li, L.; Wu, Z. L.; Zheng, Q. Ultrastiff and Tough Supramolecular Hydrogels with a Dense and Robust Hydrogen Bond Network. *Chem. Mater.* **2019**, *31*, 1430−1440.

(17) Gao, H.; Zhao, Z.; Cai, Y.; Zhou, J.; Hua, W.; Chen, L.; Wang, L.; Zhang, J.; Han, D.; Liu, M.; Jiang, L. Adaptive and Freeze-Tolerant Heteronetwork Organohydrogels with Enhanced Mechanical Stability Over a Wide Temperature Range. *Nat. Commun.* **2017**, *8*, 15911.

(18) Rong, Q.; Lei, W.; Chen, L.; Yin, Y.; Zhou, J.; Liu, M. A.F. Anti-freezing, Conductive Self-healing Organohydrogels with Stable Strain-Sensitivity at Subzero Temperatures. *Angew. Chem., Int. Ed.* **2017**, *56*, 14159−14163.

(19) Zhao, Z.; Zhang, K.; Liu, Y.; Zhou, J.; Liu, M. Highly Stretchable, Shape Memory Organohydrogels Using Phase-Transition Microinclusions. *Adv. Mater.* **2017**, *29*, 1701695.

(20) Nguyen, T. P.; Nguyen, Q. V.; Nguyen, V.-H.; Le, T.-H.; Huynh, V. Q. N.; Vo, D.-V.; Trinh, Q. T.; Kim, S. Y.; Le, Q. V. Silk

Fibroin-Based Biomaterials for Biomedical Applications: A Review. *Polymer* **2019**, *11*, 1933.
(21) Reizabal, A.; Costa, C. M.; Pérez-Álvarez, L.; Vilas-Vilela, J. L.; Lanceros-Méndez, S. Silk Fibroin as Sustainable Advanced Material: Material Properties and Characteristics, Processing, and Applications. *Adv. Funct. Mater.* **2023**, *33*, 2210764.
(22) Zhao, Y.; Zhu, Z. S.; Guan, J.; Wu, S. J. Processing, Mechanical Properties and Bioapplications of Silk Fibroin-Based High-Strength Hydrogels. *Acta Biomater.* **2021**, *125*, 57−71.
(23) Zhao, Y.; Guan, J.; Wu, S. J. Highly Stretchable and Tough Physical Silk Fibroin−Based Double Network Hydrogels. *Macromol. Rapid Commun.* **2019**, *40*, 1900389.
(24) Jin, H. J.; Kaplan, D. L. Mechanism of silk processing in insects and spiders. *Nature* **2003**, *424*, 1057−1061.
(25) Oral, C. B.; Yetiskin, B.; Cil, C.; Kok, F. N.; Okay, O. Silk Fibroin-Based Shape-Memory Organohydrogels with Semicrystalline Microinclusions. *ACS Appl. Bio Mater.* **2023**, *6*, 1594−1603.
(26) Yetiskin, B.; Okay, O. Silk Fibroin Cryogel Building Adaptive Organohydrogels with Switching Mechanics and Viscoelasticity. *ACS Appl. Polym. Mater.* **2022**, *4*, 5234−5245.
(27) Bas, Y.; Okay, O. Mechanically Robust Shape-Memory Organohydrogels Based on Silk Fibroin with Organogel Microinclusions of Various Sizes. *Macromol. Mater. Eng.* **2023**, *308*, 2300129.
(28) Pilate, F.; Toncheva, A.; Dubois, P.; Raquez, J.-M. Shape-Memory Polymers for Multiple Applications in the Materials World. *Eur. Polym. J.* **2016**, *80*, 268−294.
(29) Earnest, C. M.; Jones, J.; Dunn, A. On the Study of Thermal Transitions in Selected n-Paraffins Using Differential Scanning Calorimetry. *Thermo* **2022**, *2*, 302−311.
(30) Kurt, B.; Gulyuz, U.; Demir, D. D.; Okay, O. High-strength semi-crystalline hydrogels with self-healing and shape memory functions. *Eur. Polym. J.* **2016**, *81*, 12−23.
(31) Miyazaki, T.; Kaneko, T.; Gong, J. P.; Osada, Y. Effects of Carboxyls Attached at Alkyl Side Chain Ends on the Lamellar Structure of Hydrogels. *Macromolecules* **2001**, *34*, 6024−6028.
(32) Truong, V. X.; Tsang, K. M.; Forsythe, J. S. Nonswelling Click-Cross-Linked Gelatin and PEG Hydrogels with Tunable Properties Using Pluronic Linkers. *Biomacromolecules* **2017**, *18*, 757−766.
(33) Ding, H.; Li, B.; Liu, Z.; Liu, G.; Pu, S.; Feng, Y.; Jia, D.; Zhou, Y. Nonswelling Injectable Chitosan Hydrogel via UV Crosslinking Induced Hydrophobic Effect for Minimally Invasive Tissue Engineering. *Carbohydr. Polym.* **2021**, *252*, 117143.
(34) Karakutuk, I.; Ak, F.; Okay, O. Diepoxide-Triggered Conformational Transition of Silk Fibroin: Formation of Hydrogels. *Biomacromolecules* **2012**, *13*, 1122−1128.
(35) Ak, F.; Oztoprak, Z.; Karakutuk, I.; Okay, O. Macroporous Silk Fibroin Cryogels. *Biomacromolecules* **2013**, *14*, 719−727.
(36) Su, E.; Bilici, C.; Bayazit, G.; Ide, S.; Okay, O. Solvent-Free UV Polymerization of n-Octadecyl Acrylate in Butyl Rubber: A Simple Way to Produce Tough and Smart Polymeric Materials at Ambient Temperature. *ACS Appl. Mater. Interfaces* **2021**, *13*, 21786−21799.
(37) Rubin, I. D.; Pugliese, R. D. A. A study of blends of poly(n-octadecyl methacrylate) with n-dodecane and n-octadecane. *Angew. Makromol. Chem.* **1989**, *171*, 165−173.
(38) Pan, X.; Wang, Q.; Ning, D.; Dai, L.; Liu, K.; Ni, Y.; Chen, L.; Huang, L. Ultraflexible Self-Healing Guar Gum-Glycerol Hydrogel with Injectable, Antifreeze, and Strain-Sensitive Properties. *ACS Biomater. Sci. Eng.* **2018**, *4*, 3397−3404.
(39) Han, L.; Liu, K.; Wang, M.; Wang, K.; Fang, L.; Chen, H.; Zhou, J.; Lu, X. Mussel-Inspired Adhesive and Conductive Hydrogel with Long-Lasting Moisture and Extreme Temperature Tolerance. *Adv. Funct. Mater.* **2018**, *28*, 1704195.

https://doi.org/10.1021/acsami.4c12648
ACS Appl. Mater. Interfaces 2024, 16, 56146−56158